Journal of Power Sources 597 (2024) 234115

Contents lists available at ScienceDirect

Journal of Power Sources

journal homepage: www.elsevier.com/locate/jpowsour

Oxygen nonstoichiometry, electrical conductivity, and electrochemical activity of $La_{0.45}Ce_{0.05}Sr_{0.5}FeO_{3-\delta}$

S.S. Nikitin [a,b,*], M.S. Dyakina [a], E.V. Tsipis [a], M.V. Patrakeev [a]

[a] Osipyan Institute of Solid State Physics RAS, Chernogolovka, Moscow Distr., 142432, Russia
[b] Institute of Solid State Chemistry and Mechanochemistry SB RAS, 630090, Novosibirsk, Novosibirsk region, Kutateladze, 18, Russia

HIGHLIGHTS

- The introduction of cerium improves sinterability and thermomechanical properties.
- Cerium incorporation increases concentration of Fe^{2+} ions and ion conductivity.
- Electrode performance evaluated both under anodic and cathodic polarization.
- $La_{0.45}Ce_{0.05}Sr_{0.5}FeO_{3-\delta}$ electrode exhibits higher activity in the SOEC mode.

ARTICLE INFO

Keywords:
Perovskite
Ce-doped lanthanum-strontium ferrite
Defect structure
Conductivity
Thermal expansion
SOFC/SOEC electrode

ABSTRACT

The crystal structure, thermal expansion, oxygen nonstoichiometry, electrical conductivity, and electrode properties under anodic and cathodic polarization of perovskite-type oxide $La_{0.45}Ce_{0.05}Sr_{0.5}FeO_{3-\delta}$ have been investigated. The oxygen content data measured in a wide range of oxygen partial pressure by coulometric titration were used to analyze the defect chemistry of the ferrite and calculate the concentrations of charge carriers. The obtained results were compared with similar available data for $La_{0.5}Sr_{0.5}FeO_{3-\delta}$. It was found that the incorporation of cerium into the lattice of the ferrite improves the sinterability of ceramics and enhances its thermomechanical properties. In addition, cerium substitution increases the concentration of Fe^{2+} ions and enhances the mobility of oxygen ions. The oxygen ion conductivity in $La_{0.45}Ce_{0.05}Sr_{0.5}FeO_{3-\delta}$ was found to be relatively high (achieves 0.5 S cm^{-1} at 950 °C) that is favorable for the use of these materials as air electrodes of solid oxide fuel and electrolysis cells. In air, porous electrode layers show significantly higher electrochemical activity in the electrolyzer mode compared to the fuel cell mode.

1. Introduction

In recent years, solid oxide electrolysis cells (SOECs) operating at elevated temperatures have received much attention. The cause of the interest is the highest efficiency of SOECs among other types of electrolysis devices in production of hydrogen, which is considered a key component of future energy system [1–3]. Although SOEC can be regarded as a reversed solid oxide fuel cell (SOFC), these two devices operate in different modes, so their electrode materials have different requirements. For instance, composites based on lanthanum-strontium manganites (LSM) with perovskite-type structure are widely used as air electrode of SOFC. However, under anodic polarization, these electrodes can undergo delamination, resulting in irreversible degradation of SOEC performance [4–6]. The mechanism of this process is associated with the formation of high local gradients of oxygen chemical potential at the electrolyte – air electrode boundary. Owing to a poor oxygen-ion conductivity, the LSM-based electrode cannot provide necessary rate of the oxygen removal from the interface that leads to the electrode delamination. Therefore, considerable efforts are focused on the development of air electrode for SOEC with suitable level of oxygen-ion conductivity in combination with high enough electron conductivity.

One promising group of oxides for air electrode development refers to perovskite-type $La_{1-x}Sr_xFeO_{3-\delta}$, where the highest level of electron and oxygen-ion transport is observed at $x \approx 0.5$ [7–9]. Ion conductivity in $La_{0.5}Sr_{0.5}FeO_{3-\delta}$ at 900 °C was reported to be ~0.3 S cm^{-1} [10]. This value exceeds ion conductivity of yttria-stabilized zirconia and

* Corresponding author. Osipyan Institute of Solid State Physics RAS, Chernogolovka, Moscow Distr., 142432, Russia.
E-mail address: nikitin@issp.ac.ru (S.S. Nikitin).

https://doi.org/10.1016/j.jpowsour.2024.234115
Received 2 December 2023; Received in revised form 11 January 2024; Accepted 22 January 2024
Available online 31 January 2024

scandia-stabilized zirconia, which are widely used as electrolytes in SOECs [11]. Since air electrode of $La_{0.5}Sr_{0.5}FeO_{3-\delta}$ should not hamper oxygen transport through the electrolyte – electrode interface, the delamination problem is expected to disappear. This material, however, exhibits excessively high thermal expansion attributed to the significant contribution of chemical expansion [10]. Another disadvantage of ferrites, limiting their use as electrode materials, is their insufficient catalytic activity in the oxygen reduction reaction [12]. One approach to solve these problems is an appropriate partial substitution of cations in the A- or B-sublattices. For instance, the incorporation of even small amounts of cerium cations into the ferrite lattice was reported to reduce the thermal expansion coefficient, increase the electronic conductivity, and improve the SOFCs performance [13,14]. In addition, $Ce_{0.1}Sr_{0.9}FeO_{3-\delta}$ was found to have a significant level of specific oxygen permeability, which is higher than that of $La_{1-x}Sr_xFeO_{3-\delta}$ oxides [15]. It is worth mentioning that cerium ions can also be incorporated into the B-sites of ferrites in the case of barium residing in the A-sublattice [16–18]. The cerium introduction was shown to improve the functional properties of SOFC cathodes. In particular, the area-specific polarization resistance of the $BaCe_{0.05}Fe_{0.95}O_{3-\delta}$ cathode was shown to be several times lower than that of $BaFeO_{3-\delta}$ [19]. However, barium-containing oxides have a strong disposition to water absorption, which may be an advantage for their use as cathode materials for proton-conducting SOFCs [20], but is hardly favorable for oxygen ion conducting cells, since water uptake and release induce thermomechanical strains and may lead to microstructural degradation. Another drawback of ferrites containing cerium in the B-sublattice is their moderate electrical conductivity, which, for example, in $BaCe_{0.05}Fe_{0.95}O_{3-\delta}$ at 800 °C in air is below 10 S cm^{-1}.

This study is aimed at the synthesis and evaluation of $La_{0.45}Ce_{0.05}Sr_{0.5}FeO_{3-\delta}$ in light of the possible use of this oxide as an air electrode for SOECs. The selection of the composition is conditioned by the widely known high catalytic activity of cerium-containing materials in oxygen reduction reaction [21]. At the same time, the precaution is taken into account, that an excessive cerium content is detrimental due to the segregation of cerium oxide [13]. Besides, it is taken into consideration that the highest electrical conductivity in $Sr_{1-a}Ce_aFe_{0.8}Co_{0.2}O_{3-x}$ in air was registered for the composition a = 0.05, whereas an increase in cerium content up to a = 0.1 leads to a threefold decrease in conductivity [22]. The crystal structure, oxygen content, defect equilibria, ionic and electronic transport, and electrode properties were examined in a wide range of experimental conditions. The obtained results were compared with the respective available data for $La_{0.5}Sr_{0.5}FeO_{3-\delta}$ to evaluate the impact of cerium introduction.

2. Materials and methods

The synthesis of $La_{0.45}Ce_{0.05}Sr_{0.5}FeO_{3-\delta}$ oxide was carried out by the citrate-nitrate auto-combustion method using metallic iron (99.995 % purity), lanthanum nitrate hexahydrate (99.9 %), cerium nitrate hexahydrate (99.6 %), and strontium nitrate (99.8 %) as starting materials. Iron was preliminarily converted into the nitrate form by dissolving in the required amount of nitric acid (analytical grade). The reagents taken in stoichiometric amounts were dissolved in bi-deionized water. Citric acid (99.9 %) was added in a proportion of 2 mol per mole of metal atom, and the pH of the solution was adjusted to pH = 7 by adding ammonium hydroxide (25 %, analytical grade), then the mixture was stirred and heated until self-ignition occurred. Throughout the entire process, no precipitation was observed, and the system remained homogeneous. The resulting gray ashes were collected and annealed at 900 °C for 10 h in order to remove residual organic matter and carbon.

Ceramic disks with a diameter of ~20 mm and a thickness of ~2.5 mm were fabricated from powdered oxide by uniaxial pressing and sintering at 1300 °C. The density of the samples was estimated from their mass and geometry. Rectangular bars with the size of about 2 mm × 2 mm × 15 mm were cut from the ceramic disks to be used for the measurements of electrical conductivity and thermal expansion, as well as for scanning electron microscopy (SEM), while the remaining ceramics were milled into powder, which was used for the X-ray diffraction (XRD) analysis and coulometric titration.

The phase composition was examined by XRD at room temperature using SmartLab Se Rigaku diffractometer (Rigaku Corporation, Japan) with monochromatic CuKα radiation. The X-ray diffraction patterns were analyzed by the Rietveld refinement method for single-phase samples and Le Bail refinement method for multi-phase samples using the GSAS-II program [23]. The SEM on a Supra 50VP microscope (Carl Zeiss, Germany) was used for the examination of the morphology of ceramics and porous electrode layers. For the SEM analysis, the ceramic samples were polished and thermally etched at 1200 °C for 1 h to obtain clearly distinguishable grain boundaries. The thermal expansion measurements were carried out using a vertical alumina dilatometer Linseis L75 (Linseis, Germany) at a heating/cooling rate of 3 °C/min in flowing air with a flow rate of 50 mL/min.

The oxygen content in the oxide, depending on temperature and oxygen partial pressure (p_{O_2}), was determined by coulometric titration in a double electrochemical cell [24]. A necessary condition for recording experimental data was to achieve equilibrium between the oxide sample and the surrounding atmosphere. The absolute value of the rate of change in the logarithm of p_{O_2} less than 10^{-4} per minute and the standard error of the mean not exceeding 0.03 % at a fixed temperature and p_{O_2} above the sample were used as equilibrium criteria.

The total electrical conductivity of the sample was measured as a function of oxygen partial pressure at different temperatures using the four-probe direct current method in the p_{O_2} range from 10^{-21} to 0.3 atm at 750–950 °C [25]. The equilibrium criteria for conductivity measurements were the absolute value of the rate of change in the logarithm of conductivity less than 10^{-5} per minute at a fixed temperature and oxygen partial pressure above the sample, as well as the standard errors of the mean not exceeding 0.25 % for conductivity and 0.05 % for p_{O_2}. The range of p_{O_2} from ~10^{-10} to 10^{-4} atm was excluded from the measurements due to the extremely slow equilibration, as was previously shown in Ref. [26].

The electrode performance was tested employing half-cells with 1.0 mm thick solid oxide electrolyte membrane of 10 mol.% Sc_2O_3 and 1 mol.% Y_2O_3 co-stabilized ZrO_2 (10Sc1YSZ, Terio, China). The inks of $La_{0.45}Ce_{0.05}Sr_{0.5}FeO_{3-\delta}$ or $Ce_{0.9}Gd_{0.1}O_{1.95}$ (GDC10) were prepared by mixing of ball-milled powders with a V-006A binder (Heraeus, Germany). In order to prevent chemical interaction between the electrode and electrolyte materials, a protective GDC10 interlayer (semicircular with geometric area of 1.2 cm^2) was first screen-printed onto one side of solid electrolyte disc and dried in air at 100 °C. Then $La_{0.45}Ce_{0.05}Sr_{0.5}FeO_{3-\delta}$ working electrode (WE) layer was deposited. After drying, the electrodes were sintered in air at 1200 °C for 2 h. The thicknesses of the interlayer and electrode layer were 6 and 25 μm, respectively (Fig. 7). The total sheet density was 9.6 mg/cm^2. Platinum counter electrode (CE) was applied on the opposite side of the solid electrolyte symmetrically to the WE. Pt reference electrode (RE) (1 mm in diameter) was placed at a distance of at least 6 mm from the WE. The CE and RE were fired in air at 950 °C for 30 min. The electrode overpotential (η) and polarization resistance (R_η) as a function of current density (i) were measured by the three-electrode technique in potentiostatic mode using an Autolab 302 N PGStat instrument equipped with FRA32 module (Metrohm Autolab B.V., The Netherlands) at 850 °C. A schematic drawing of the experimental set-up for the electrode polarization measurements is shown in Fig. S1 of Supplementary material. The relaxation time after changing the WE potential was 60 min. The values of ohmic and polarization resistances were determined from the impedance spectra collected in the frequency range from 0.1 Hz to 1 MHz. In order to clarify the possibility of a potential interaction between $La_{0.45}Ce_{0.05}Sr_{0.5}FeO_{3-\delta}$ and a protective GDC10 interlayer, the corresponding powders were thoroughly mixed and subjected to two heat treatment regimes. The first mode corresponded to the sintering of

electrodes (1200 °C for 2 h), whilst the second simulated the operating conditions (850 °C for 100 h). After cooling, both samples were ground for XRD analysis.

3. Results and discussion

3.1. Structure and lattice expansion

The X-ray diffraction data Rietveld refinement of synthesized $La_{0.45}Ce_{0.05}Sr_{0.5}FeO_{3-\delta}$ shown in Fig. 1a testify the formation of a single-phase oxide with orthorhombic symmetry (S.G. *Pbnm*) in contrast to rhombohedral symmetry (S.G. $R\bar{3}c$) of cerium-free $La_{0.5}Sr_{0.5}FeO_{3-\delta}$. The pseudocubic perovskite unit cell parameter of $La_{0.45}Ce_{0.05}Sr_{0.5}FeO_{3-\delta}$ (a_p = 3.8878(2) Å) is identical to that of $La_{0.5}Sr_{0.5}FeO_{3-\delta}$ (a_p = 3.888 Å) [27], within the limits of experimental error, although the radius of Ce^{4+} (R_{CN12} = 1.14 Å) is smaller than the radius of La^{3+} (R_{CN12} = 1.36 Å) [28]. This behavior should be attributed to the reduction of Fe^{4+} ions (R_{CN6} = 0.585 Å) to larger Fe^{3+} ions (R_{CN6} = 0.645 Å) due to charge compensation upon replacement of La^{3+} with Ce^{4+} as in the case of similar perovskite-type oxides [29]. After annealing $La_{0.45}Ce_{0.05}Sr_{0.5}FeO_{3-\delta}$ oxide at 950 °C and oxygen partial pressure of ~10^{-10} atm the orthorhombic structure is retained (Fig. 1b), whilst the pseudocubic unit cell parameter becomes higher (a_p = 3.8902 Å).

The estimated density of the $La_{0.45}Ce_{0.05}Sr_{0.5}FeO_{3-\delta}$ ceramic sample, sintered in air at 1300 °C, is about 98 % of the theoretical value calculated from the XRD results. Fig. S2 in Supplementary materials presents SEM image, which confirms the formation of ceramics with high density and grain size varying in the range of 1–5 μm. It should be noted that the $La_{0.5}Sr_{0.5}FeO_{3-\delta}$ ceramics, sintered at 1300 °C, had the relative density of only 65.1 %, whereas the density of 93.1 % is achieved after sintering at 1500 °C [27]. Thus, the introduction of a small amount of cerium into the A-sublattice of $La_{0.5}Sr_{0.5}FeO_{3-\delta}$ improves the sinterability, which may be advantageous for the formation of SOFC/SOEC electrode layers.

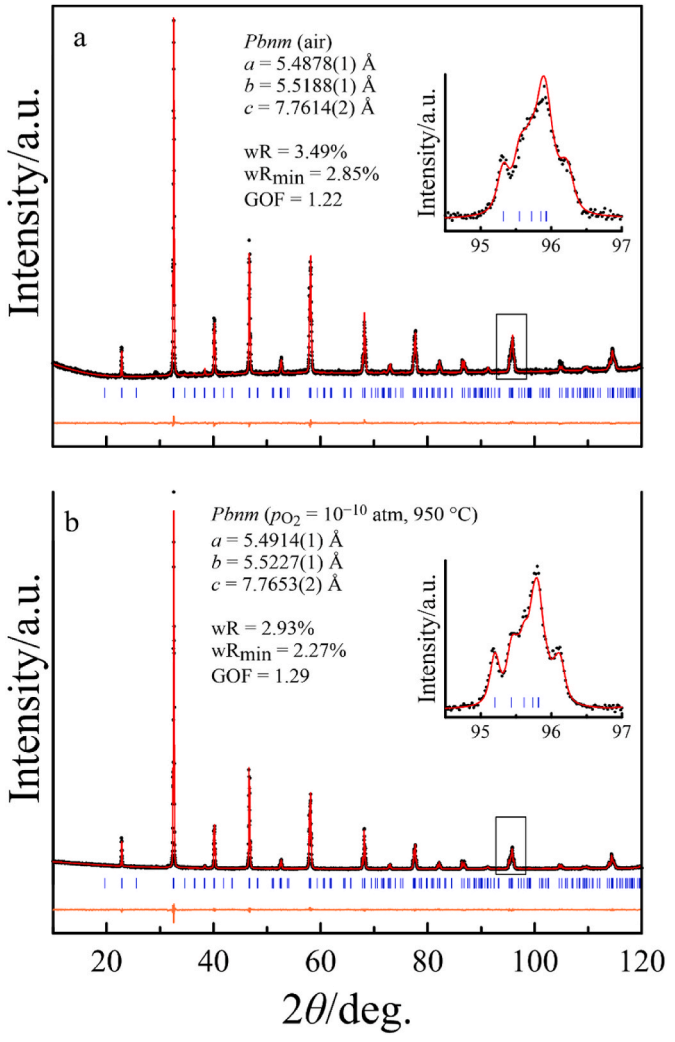

Fig. 1. Room-temperature X-ray powder diffraction patterns of $La_{0.45}Ce_{0.05}Sr_{0.5}FeO_{3-\delta}$ as-prepared (a) and after reductive treatment at 950 °C and oxygen partial pressure of ~10^{-10} atm (b).

The dilatometric curve recorded in air (Fig. 2) has two clearly visible linear parts, corresponding to the average linear thermal expansion coefficients (TECs) of $12{\cdot}10^{-6}$ K^{-1} (100–400 °C) and $23{\cdot}10^{-6}$ K^{-1} (700–1000 °C). The higher TEC values at elevated temperatures are typical for perovskite-type oxides with variable oxygen content and are explained by the contribution of chemical expansion attributed to the oxygen release from the lattice on heating and to the corresponding decrease in cation oxidation states [30,31]. This agrees with the data on oxygen nonstoichiometry and total electrical conductivity, discussed below. It is worth noting that, although the obtained TEC values are excessively high for the SOFC/SOEC electrode applications, they are lower than those of $La_{0.5}Sr_{0.5}FeO_{3-\delta}$ ($14{\cdot}10^{-6}$ K^{-1} (120–680 °C) and $26{\cdot}10^{-6}$ K^{-1} (700–880 °C) [32]) in the whole temperature range. Thus, partial substitution of cerium for lanthanum in $La_{0.5}Sr_{0.5}FeO_{3-\delta}$ improves thermomechanical properties in accordance with the oxygen content variations. For the sake of comparison, the dilatometric data for $La_{0.5}Sr_{0.4}Ca_{0.1}FeO_{3-\delta}$ [33], $La_{0.5}Sr_{0.5}Fe_{0.9}Ti_{0.1}O_{3-\delta}$ [9], and $La_{0.5}Sr_{0.5}Fe_{0.9}Al_{0.1}O_{3-\delta}$ [34] ceramics are also presented in Fig. 2. The introduction of Ti^{4+} provides the most favorable effect on thermomechanical properties of $La_{0.5}Sr_{0.5}FeO_{3-\delta}$. These results demonstrate once again that, at temperatures above 500 °C, the thermal expansion is affected by oxygen release from the lattice, which in turn depends to a considerable degree on the oxidation state of the dopant and its concentration.

3.2. Defect chemistry

Fig. 3 presents isotherms of the oxygen content in $La_{0.45}Ce_{0.05}Sr_{0.5}FeO_{3-\delta}$ as a function of oxygen partial pressure. The experimental data are shown by symbols. For the sake of comparison,

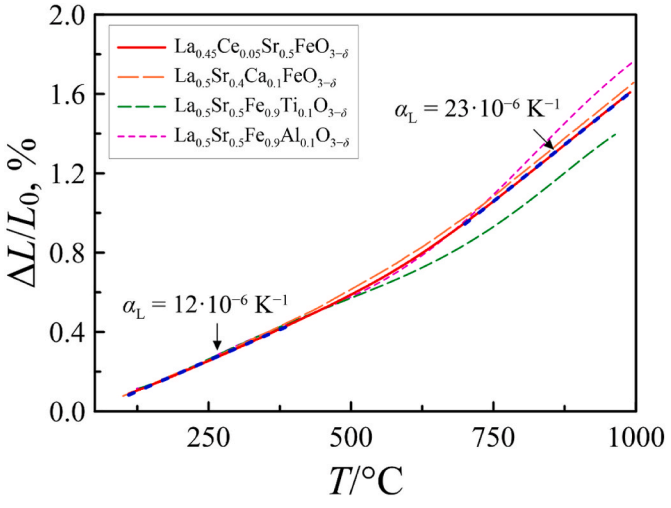

Fig. 2. Relative elongation of a ceramic sample of $La_{0.45}Ce_{0.05}Sr_{0.5}FeO_{3-\delta}$ as a function of temperature. Blue lines represent linear fit in temperature regions of 100–400 °C and 700–1000 °C. α_L denotes the coefficient of linear thermal expansion. The literature data for the $La_{0.5}Sr_{0.5}FeO_{3-\delta}$ ferrite substituted by Ca, Ti, and Al are taken from Refs. [9,33], and [34], respectively. (For interpretation of the references to colour in this figure legend, the reader is referred to the Web version of this article.)

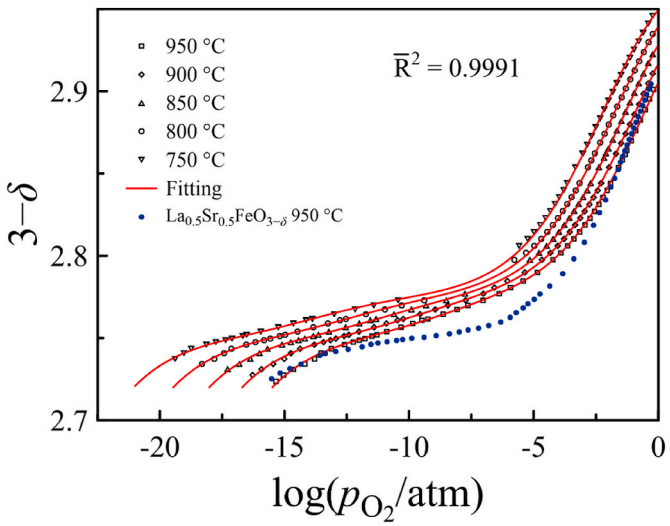

Fig. 3. Oxygen content in $La_{0.45}Ce_{0.05}Sr_{0.5}FeO_{3-\delta}$ versus the logarithm of oxygen partial pressure at different temperatures. Data for $La_{0.5}Sr_{0.5}FeO_{3-\delta}$ at 950 °C are taken from Ref. [27]. Solid lines represent the results of calculation according to equation (5).

isotherm of oxygen content in $La_{0.5}Sr_{0.5}FeO_{3-\delta}$ at 950 °C is depicted in the figure as well. There is a clearly seen plateau-like region on the isotherm of $La_{0.5}Sr_{0.5}FeO_{3-\delta}$ where the oxygen content depends weakly on the oxygen partial pressure. The introduction of even 5 mol. % of cerium in A-sublattice alters the shape of the curves, leading to their smooth decrease with decreasing oxygen partial pressure. To understand the occurring processes, experimental data were used for thermodynamic modeling of the defect equilibrium in the oxide.

To describe the oxygen content data, a point defect model similar to that for $La_{0.5}Sr_{0.5}Fe_{0.9}Mo_{0.1}O_{3-\delta}$ [35] and $Sr_{1-x}Ce_xFeO_{3-\delta}$ [36] was used, which assumes the formation of defects as a result of three reactions: iron oxidation (1), charge disproportionation on iron ions (2), and electron exchange between iron and cerium ions (3):

$$\frac{1}{2}O_2 + V_O + 2Fe^{3+} \rightleftarrows O^{2-} + 2Fe^{4+} \quad K_{ox} = \frac{[O^{2-}][Fe^{4+}]^2}{\sqrt{p_{O_2}}[V_O][Fe^{3+}]^2} \tag{1}$$

$$2Fe^{3+} \rightleftarrows Fe^{4+} + Fe^{2+} \quad K_d = \frac{[Fe^{4+}][Fe^{2+}]}{[Fe^{3+}]^2} \tag{2}$$

$$Fe^{3+} + Ce^{3+} \rightleftarrows Fe^{2+} + Ce^{4+} \quad K_e = \frac{[Fe^{2+}][Ce^{4+}]}{[Fe^{3+}][Ce^{3+}]} \tag{3}$$

where K_{ox}, K_d and K_e are the equilibrium constants of the corresponding reactions.

The relationship between equilibrium constants of the defect formation reaction and related thermodynamic parameters can be expressed via a well-known thermodynamic equation:

$$K_i = \exp\left(-\frac{\Delta G_i^0}{RT}\right) = \exp\left(-\frac{\Delta H_i^0}{RT} + \frac{\Delta S_i^0}{R}\right) \tag{4}$$

where R is the gas constant, ΔG_i^0, ΔH_i^0, ΔS_i^0, are the standard free Gibbs energy, enthalpy, and entropy for the defect formation reactions, respectively.

Two additional parameters are introduced in the model: $\Delta\delta_{ref}$ serves to accurately adjust the experimental data of oxygen content for minimization of calculation errors, and w denotes the number of anion positions per formula unit that are inaccessible to oxygen ions. The latter parameter can reflect the action of various factors, which in some cases are not obvious; nevertheless, its consideration helps to achieve the best results in simulation of oxygen content data. For instance, the appearance of unoccupied vacancies in oxide series of $Sr_{1-x}Ce_xFeO_{3-\delta}$ was reported to be attributed to steric disturbances due to the replacement of strontium by cerium, which has a significantly smaller size [36].

The joint solution of equations (1)–(4) with taking into account the conditions of site conversion and electroneutrality allows obtaining the final model equation in the form:

$$5.55 - \frac{K_d - K_{ox}T_s}{K_d + K_{ox}T_s + \sqrt{K_{ox}T_s}} - \frac{K_d}{20\left(K_d + K_e\sqrt{K_{ox}T_s}\right)} = 2\left(3 - \delta + \Delta\delta_{ref}\right) \tag{5}$$

where $T_s = \frac{\delta - w - \Delta\delta_{ref}}{3 - \delta + \Delta\delta_{ref}} \cdot \sqrt{p_{O_2}}$. More detailed information on the derivation of this equation can be found in the Supplementary Materials. The Levenberg-Marquardt algorithm of LMFIT library [37] in a program specially written for this purpose in Python was used for the approximation of equation (5) to the experimental data.

Fig. 3 demonstrates good agreement between experimental data on oxygen content in $La_{0.45}Ce_{0.05}Sr_{0.5}FeO_{3-\delta}$ and the results of model calculations depicted by solid lines. This, in combination with a high value of the adjusted coefficient of determination ($\bar{R}^2$), confirms the adequacy of the used model and obtained parameters collected in Table 1.

According to the results of calculations, cerium introduction into A-sublattice causes some increase in the enthalpy of oxidation and charge disproportionation reactions. Nevertheless, the main difference in the shape of $La_{0.5}Sr_{0.5}FeO_{3-\delta}$ and $La_{0.45}Ce_{0.05}Sr_{0.5}FeO_{3-\delta}$ isotherms is attributed to the action of electron exchange reaction between iron and cerium. Thermodynamic parameters of this reaction indicate that Ce^{4+} is less stable to reduction than Fe^{3+}. Therefore, under the condition of stable Fe^{3+} concentration in $La_{0.5}Sr_{0.5}FeO_{3-\delta}$, corresponding to plateau on oxygen content isotherm, reduction of cerium in $La_{0.45}Ce_{0.05}Sr_{0.5}FeO_{3-\delta}$ accompanies a decrease in oxygen content, causing a tilt of the respective isotherm part.

In Fig. 4, the concentrations of iron and cerium ions in $La_{0.45}Ce_{0.05}Sr_{0.5}FeO_{3-\delta}$ in different oxidation states versus oxygen partial pressure at different temperatures are shown together with similar data for $La_{0.5}Sr_{0.5}FeO_{3-\delta}$ at 950 °C drawn for comparison from Ref. [27]. The incorporation of cerium is seen to lead to an increase in the concentration of Fe^{2+} ions and a decrease in the concentration of Fe^{4+} ions in the oxide.

3.3. Electrical conductivity

The experimental data on the total electrical conductivity (σ) variations in $La_{0.45}Ce_{0.05}Sr_{0.5}FeO_{3-\delta}$ with oxygen partial pressure and temperature are shown in Fig. 5. The data for $La_{0.5}Sr_{0.5}FeO_{3-\delta}$ [27], $La_{0.5}Sr_{0.4}Ca_{0.1}FeO_{3-\delta}$ [33], $La_{0.5}Sr_{0.5}Fe_{0.9}Ti_{0.1}O_{3-\delta}$ [9], and $La_{0.5}Sr_{0.5}Fe_{0.9}Al_{0.1}O_{3-\delta}$ [34] at 950 °C are also given for comparison. Under oxidizing conditions, low concentrations of selected dopants have little effect on conductivity. The effect of doping becomes, however, more pronounced under reducing conditions. The conductivity isotherms of $La_{0.5}Sr_{0.5}FeO_{3-\delta}$ and $La_{0.5}Sr_{0.4}Ca_{0.1}FeO_{3-\delta}$ under reducing conditions are almost merging since the substitution of calcium for strontium leaves unchanged the Fe–O subsystem providing the

Table 1
Thermodynamic parameters of defect formation reactions.

Parameter	$La_{0.45}Ce_{0.05}Sr_{0.5}FeO_{3-\delta}$	$La_{0.5}Sr_{0.5}FeO_{3-\delta}$ from [27]
ΔH_{ox}^0/kJ·mol^{-1}	−99.9 ± 0.3	−107 ± 2
ΔS_{ox}^0/J·mol^{-1}K^{-1}	−67.5 ± 0.3	−70 ± 2
ΔH_d^0/kJ·mol^{-1}	117 ± 1	111 ± 2
ΔS_d^0/J·mol^{-1}K^{-1}	−3.8 ± 0.2	8 ± 2
ΔH_e^0/kJ·mol^{-1}	17.9 ± 0.4	
ΔS_e^0/J·mol^{-1}K^{-1}	−39.5 ± 0.8	
w•10^3	27.9 ± 0.3	

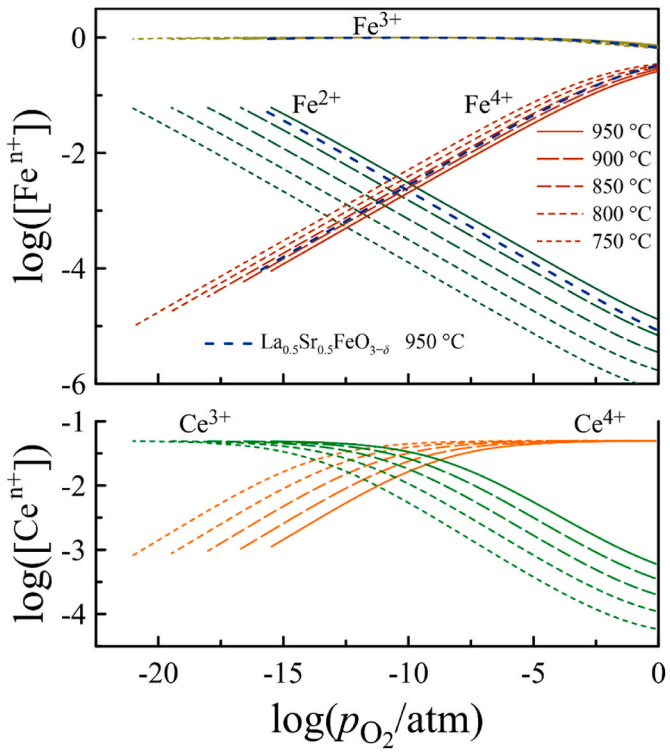

Fig. 4. Concentrations of iron and cerium ions in different oxidation states in $La_{0.45}Ce_{0.05}Sr_{0.5}FeO_{3-\delta}$ as functions of oxygen partial pressure at different temperatures. Data for $La_{0.5}Sr_{0.5}FeO_{3-\delta}$ are taken from Ref. [27].

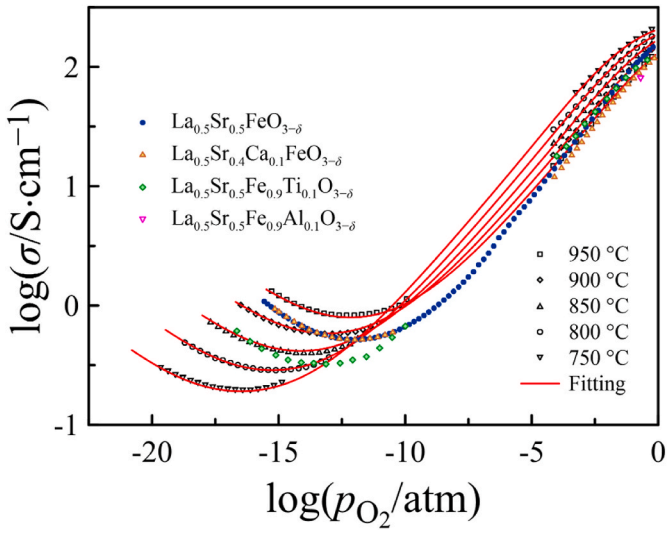

Fig. 5. Electrical conductivity of $La_{0.45}Ce_{0.05}Sr_{0.5}FeO_{3-\delta}$ versus the logarithm of oxygen partial pressure at different temperatures. Solid lines represent the results of calculation according to equation (6). Conductivity data for $La_{0.5}Sr_{0.5}FeO_{3-\delta}$, $La_{0.5}Sr_{0.4}Ca_{0.1}FeO_{3-\delta}$, $La_{0.5}Sr_{0.5}Fe_{0.9}Ti_{0.1}O_{3-\delta}$, and $La_{0.5}Sr_{0.5}Fe_{0.9}Al_{0.1}O_{3-\delta}$ at 950 °C are taken from Refs. [9,27,33], and [34], respectively.

pathways of electron transport. Titanium, which under experimental conditions retains constant oxidation state 4+, disrupts the pathways of electrons in the Fe–O framework, which makes the conductivity of $La_{0.5}Sr_{0.5}Fe_{0.9}Ti_{0.1}O_{3-\delta}$ lower than that of $La_{0.5}Sr_{0.5}FeO_{3-\delta}$. In contrast, the conductivity of $La_{0.45}Ce_{0.05}Sr_{0.5}FeO_{3-\delta}$ exceeds that of undoped oxide except for the high-p_{O_2} range. In order to elucidate the reason for this behavior, the obtained results were analyzed, taking into account the participation of oxygen ions, electrons, and electron-holes in the charge transfer, as it is typical for perovskite-type ferrites.

Several models were considered for the conductivity simulation, similarly to the work [38]. The best agreement with the experimental data was obtained, however, for a model neglecting the involvement of cerium ions in electronic transport. This can be explained by the extremely low cerium content and by the large Ce–O–Ce distance compared to that of Fe–O–Fe (2.478 Å and 1.917 Å, respectively).

Briefly, the approach can be expressed by the following system of equations 6–10:

$$\sigma = \sigma_i + \sigma_n + \sigma_p \tag{6}$$

$$\sigma_i = N \cdot e \cdot 2 \cdot (3-\delta) \cdot \mu_i, \mu_i = \mu_i^0 \cdot (\delta - w) \tag{7}$$

$$\sigma_n = N \cdot e \cdot [Fe^{2+}] \cdot \mu_n,\ \mu_n = \mu_n^0 \cdot [Fe^{3+}] \tag{8}$$

$$\sigma_p = N \cdot e \cdot [Fe^{4+}] \cdot \mu_p,\ \mu_p = [Fe^{3+}] \cdot \left(\mu_p^0 + \mu_p^1 [Fe^{4+}] + \mu_p^2 [Fe^{4+}]^2\right) \tag{9}$$

where N is the number of $La_{0.45}Ce_{0.05}Sr_{0.5}FeO_{3-\delta}$ unit cells per unit volume; e is the elementary charge; multiplier 2 takes into account the charge of oxygen ion; σ_i, σ_n, σ_p are the oxygen ion, electron, and hole conductivity, respectively; μ_i, μ_n, μ_p are the mobilities of oxygen ions, electrons, and holes, respectively; μ_i^0, μ_n^0, μ_p^0, μ_p^1, μ_p^2 are constants.

$$\mu_k^0 = \frac{b_k}{T} \exp\left(-\frac{E_{\mu,k}}{k_B T}\right) \tag{10}$$

where k_B is the Boltzmann constant, $E_{\mu,k}$ and b_k are activation energy and the pre-exponential factor for the mobility of the considered type of charge carriers. Equation (9) expresses the complex dependence of hole mobility on the oxygen content in ferrites, and was shown to be appropriate in a number of previous studies [27,35,39].

The results of calculations shown in Fig. 5 by solid lines follow perfectly experimental data, thus confirming the adequacy of the used model and the reliability of the fitting parameters collected in Table 2. The obtained data allow separating the contributions of oxygen ions, electrons, and holes to the total conductivity. These results are shown in Fig. 6a together with similar data for $La_{0.5}Sr_{0.5}FeO_{3-\delta}$ at 950 °C in order to trace the effect of cerium introduction. Fig. 6b-d shows the mobilities of electrons, holes, and oxygen ions in $La_{0.45}Ce_{0.05}Sr_{0.5}FeO_{3-\delta}$ in relation to oxygen partial pressure at different temperatures, as well as similar data for $La_{0.5}Sr_{0.5}FeO_{3-\delta}$ at 950 °C. As can be clearly seen in Fig. 6a, the introduction of cerium results in an increase in the n-type conductivity due to the higher concentration of electronic charge carriers (Fig. 4). Although the p-type conductivity in cerium-containing oxide is lower at $p_{O_2} > 10^{-3}$ atm due to the lower concentration of the respective charge carriers, a decrease in p_{O_2} leads to a predominance of the mobility effect, therefore the conductivity of $La_{0.45}Ce_{0.05}Sr_{0.5}FeO_{3-\delta}$ gradually begins to exceed that of $La_{0.5}Sr_{0.5}FeO_{3-\delta}$. The reason of why the mobility of p-type carriers in $La_{0.45}Ce_{0.05}Sr_{0.5}FeO_{3-\delta}$ is higher is probably due to larger oxygen content in this oxide that provides higher proportion of Fe–O–Fe links for hole transfer. As for the oxygen-ion conductivity, its increase upon the cerium introduction reflects an increase in the mobility of

Table 2
Parameters of conductivity data best fitting.

	$La_{0.45}Ce_{0.05}Sr_{0.5}FeO_{3-\delta}$	$La_{0.5}Sr_{0.5}FeO_{3-\delta}$ from [27]
$E_{\mu i}$/eV	0.81 ± 0.01	0.63 ± 0.03
b_i/cm^{2}V^{-1}s^{-1}K	403 ± 20	
$E_{\mu n}$/eV	0.59 ± 0.02	0.78 ± 0.04
b_n/cm^{2}V^{-1}s^{-1}K	1616 ± 107	
$E_{\mu p}$/eV	0.136 ± 0.008	0.17 ± 0.02
b_p/cm^{2}V^{-1}s^{-1}K	389 ± 16	
μ_p^1/cm^{2}V^{-1}s^{-1}	0.295 ± 0.009	
μ_p^2/cm^{2}V^{-1}s^{-1}	1.18 ± 0.02	

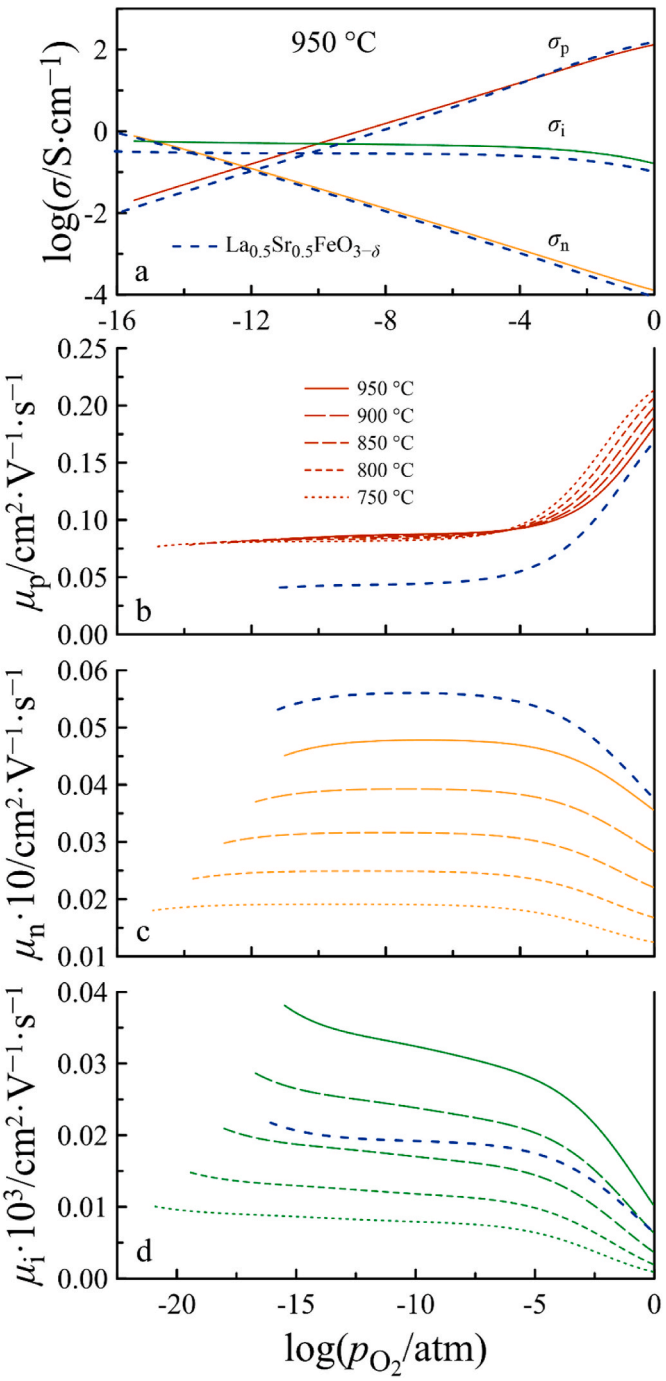

Fig. 6. Partial conductivities at 950 °C (a), and mobility of p-type carriers (b), n-type carriers (c), and oxygen ions (d) in $La_{0.45}Ce_{0.05}Sr_{0.5}FeO_{3-\delta}$ versus the logarithm of oxygen partial pressure at different temperatures. Similar data for $La_{0.5}Sr_{0.5}FeO_{3-\delta}$ at 950 °C are taken from Ref. [27].

oxygen ions, which origin is not yet clear.

In any case, a favorable effect of the cerium doping on the oxygen ionic conductivity should result in better electrode performance, especially in the SOEC mode.

3.4. Electrode properties

In order to evaluate the applicability of the $La_{0.45}Ce_{0.05}Sr_{0.5}FeO_{3-\delta}$ oxide for SOFC/SOEC air electrode, first of all, its chemical compatibility with the protective interlayer material, GDC10, was tested. The lattice parameters of pure cerium dioxide and GDC10 are 5.411 Å [40], and 5.4183 Å [41], respectively. The XRD Le Bail refinement results of a mixture of $La_{0.45}Ce_{0.05}Sr_{0.5}FeO_{3-\delta}$ and GDC10 after annealing in air at 1200 °C for 2 h (Fig. S2a) show that no secondary phases were formed. However, the unit cell of GDC10 became lower, while that of $La_{0.45}Ce_{0.05}Sr_{0.5}FeO_{3-\delta}$ increased. A similar behavior was observed for the same mixture after heat treatment at 850 °C for 100 h (Fig. S2b). Extrapolation of the data presented in Ref. [41] reveals that the nominal composition of gadolinium-doped ceria refers to 9.4 ± 0.3 mol.% Gd, indicating that a part of cerium cations from $La_{0.45}Ce_{0.05}Sr_{0.5}FeO_{3-\delta}$ might diffuse into GDC. The respective A-site cation deficiency should be beneficial for both oxygen ion and electron transport, as was previously reported for similar perovskite-type ferrites [27,42]. Thus, although the performed test revealed a sign of cation diffusion between the interlayer and electrode materials, no harmful effect of this phenomenon is anticipated.

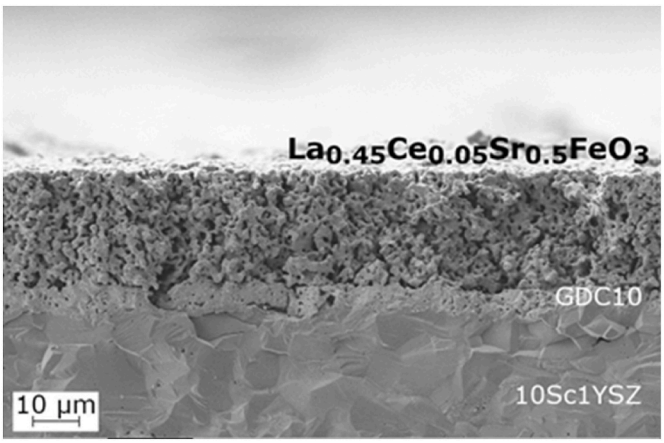

Fig. 7. SEM image of the fractured electrochemical cell with porous $La_{0.45}Ce_{0.05}Sr_{0.5}FeO_{3-\delta}$ electrode layer in contact with GDC10 interlayer deposited onto the surface of 10Sc1YSZ solid electrolyte, after electrochemical measurements.

Fig. 7 demonstrates the microstructure of a half-cell used for the test of electrode performance. The solid electrolyte has a high density, the protective interlayer, with a thickness of about 5 μm, separates reliably the electrode and electrolyte, whereas the electrode has a homogeneous microstructure formed by submicron-sized grains and a suitable porosity for gas diffusion.

Fig. 8a shows the polarization curves of $La_{0.45}Ce_{0.05}Sr_{0.5}FeO_{3-\delta}$ porous electrode layers in contact with 10Sc1YSZ solid electrolyte and GDC10 protective interlayer in air at 850 °C. The electrode overpotentials under anodic polarization are significantly lower than those under cathodic polarization. This behavior correlates with the conductivity variations (Fig. 6). Under anodic polarization, the oxygen chemical potential at the electrode surface should be higher than in the gas phase, increasing the p-type conductivity in the electrode material. If the electrode performance is limited by the electronic transport, this would lower the polarization resistance and overpotential. The difference in anodic and cathodic polarization may also originate from different mechanisms of oxygen evolution and reduction reactions, although the polarization curves are well described by the Butler-Volmer equation [43,44]:

$$i = i_0\left[\exp\left(\frac{\alpha nF\eta}{RT}\right) - \exp\left(-\frac{\beta nF\eta}{RT}\right)\right] \quad (11)$$

where n is the number of electrons participating in the rate-determining step, α and β are the charge transfer coefficients, and i_0 is related to the exchange current density. The obtained i_0 value is 10.8 ± 0.6 mA × cm^{-2}. At the same time, the impedance spectra clearly consist of two separable arcs and were modeled by two sequential processes (Fig. 8b). The high-frequency signal can be interpreted as a limiting charge

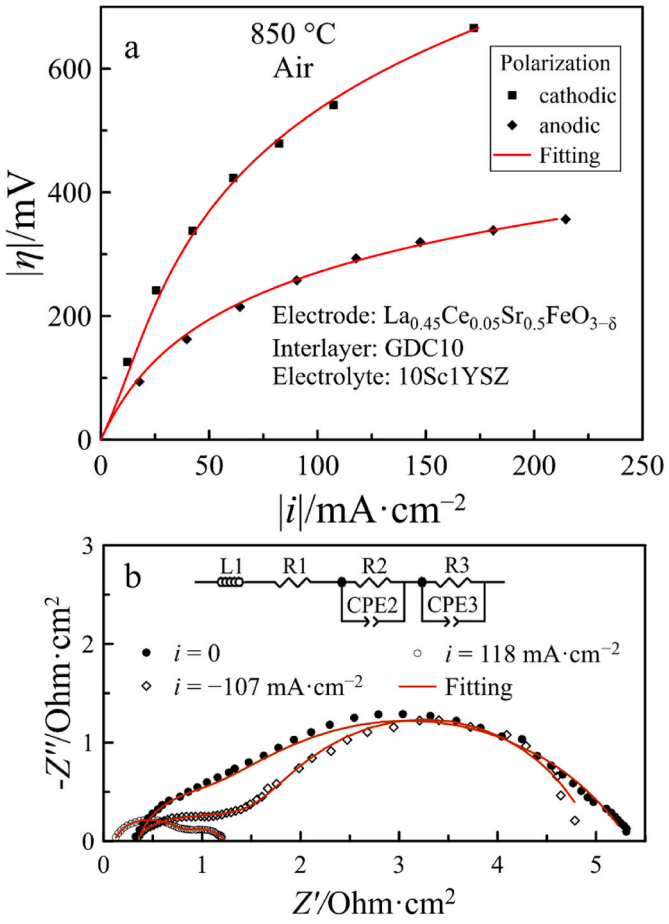

Fig. 8. Dependencies of the overpotentials of $La_{0.45}Ce_{0.05}Sr_{0.5}FeO_{3-\delta}$ porous electrode on the anodic and cathodic current density in air at 850 °C. Solid lines show the results of non-linear regression analysis using the Butler-Volmer equation (a). Impedance spectra of $La_{0.45}Ce_{0.05}Sr_{0.5}FeO_{3-\delta}$ porous electrode under open-circuit conditions and under anodic and cathodic polarization (b); solid lines show the fitting results using equivalent circuit presented in the inset.

transfer process. The signal at low frequencies is usually attributed to diffusion processes. This latter signal decreases drastically when operating in the SOEC mode, which is indicative of less important role of surface diffusion in the oxygen evolution reaction. On the contrary, the diffusion of oxygen adatoms/ions to the electrochemical reaction zone may be limiting in the case of oxygen reduction at the SOFC cathode.

Whatever the mechanisms of electrode reactions, the electrode performance is, in general, quite similar to that of the other pure and doped lanthanum ferrites [45–47]. In the case of SOEC anode, this material may be promising provided that its electronic conductivity is increased and its thermal expansion coefficients are decreased by appropriate doping. Possible strategies may include increasing cerium content, varying lanthanum to strontium ratio, and/or introducing another electroactive cation such as molybdenum.

4. Conclusions

The oxygen nonstoichiometry and electrical conductivity of $La_{0.45}Ce_{0.05}Sr_{0.5}FeO_{3-\delta}$ with the perovskite-type structure were studied in the oxygen partial pressure range from 10^{-20} to 0.3 atm at 750–950 °C. The introduction of cerium reduces the values of thermal expansion coefficients as well as provides a higher concentration of Fe^{2+} ions and greater mobility of oxygen ions compared to undoped ferrite, resulting in higher n-type and oxygen ion conductivity. The electrode performance was evaluated both under anodic and cathodic polarization via three-electrode method. The $La_{0.45}Ce_{0.05}Sr_{0.5}FeO_{3-\delta}$ porous electrode layers should preferably be used as SOEC anodes but not as SOFC cathodes when their performance is moderate. The examination of the XRD patterns of a mixture of $La_{0.45}Ce_{0.05}Sr_{0.5}FeO_{3-\delta}$ and gadolinium-doped ceria revealed the occurrence of a cation deficiency in the former, caused by the diffusion of cerium from ferrite to GDC10, which is known to provide an increase in conductivity.

CRediT authorship contribution statement

S.S. Nikitin: Writing – original draft, Visualization, Software, Formal analysis, Conceptualization. **M.S. Dyakina:** Methodology, Investigation, Formal analysis. **E.V. Tsipis:** Writing – original draft, Methodology, Investigation, Formal analysis, Conceptualization. **M.V. Patrakeev:** Writing – review & editing, Writing – original draft, Visualization, Supervision, Software, Investigation, Formal analysis, Conceptualization.

Declaration of competing interest

The authors declare that they have no known competing financial interests or personal relationships that could have appeared to influence the work reported in this paper.

Data availability

Data will be made available on request.

Acknowledgments

The authors are grateful to the Russian Science Foundation (Project 21-79-30051), for the support of this work.

Appendix A. Supplementary data

Supplementary data to this article can be found online at https://doi.org/10.1016/j.jpowsour.2024.234115.

References

[1] F. Lehner, D. Hart, Chapter 1 - the importance of water electrolysis for our future energy system, in: Tom Smolinka, Jurgen Garche, Electrochemical Power Sources: Fundamentals, Systems, and Applications, Elsevier, 2022, pp. 1–36, https://doi.org/10.1016/B978-0-12-819424-9.00008-2.

[2] S.E. Wolf, F.E. Winterhalder, V. Vibhu, O. Guillon, R.-A. Eichel, N.H. Menzler, Solid oxide electrolysis cells – current material development and industrial application, J. Mater. Chem. A 11 (2023) 17977, https://doi.org/10.1039/D3TA02161K.

[3] W. Kreuter, H. Hofmann, Electrolysis: the important energy transformer in a world of sustainable energy, Int. J. Hydrogen Energy 23 (1998) 661–666, https://doi.org/10.1016/S0360-3199(97)00109-2.

[4] S.J. McPhail, S. Frangini, J. Laurencin, E. Effori, A. Abaza, A.K. Padinjarethil, A. Hagen, A. Léon, A. Brisse, D. Vladikova, B. Burdin, F.R. Bianchi, B. Bosio, P. Piccardo, R. Spotorno, H. Uchida, P. Polverino, E.A. Adinolfi, F. Postiglione, J.-H. Lee, H. Moussaoui, J. Van herle, Addressing planar solid oxide cell degradation mechanisms: a critical review of selected components, Electrochem Sci Adv 2 (2022) e2100024, https://doi.org/10.1002/elsa.202100024.

[5] A.V. Virkar, Mechanism of oxygen electrode delamination in solid oxide electrolyzer cells, Int. J. Hydrogen Energy 35 (2010) 9527–9543, https://doi.org/10.1016/j.ijhydene.2010.06.058.

[6] M.S. Khan, X. Xu, R. Knibbe, Z. Zhu, Air electrodes and related degradation mechanisms in solid oxide electrolysis and reversible solid oxide cells, Renew. Sustain. Energy Rev. 143 (2021) 110918, https://doi.org/10.1016/j.rser.2021.110918.

[7] J.A. Bahteeva, I.A. Leonidov, M.V. Patrakeev, E.B. Mitberg, V.L. Kozhevnikov, K.R. J. Poeppelmeier, High-temperature ion transport in $La_{1-x}Sr_xFeO_{3-\delta}$, J. Solid State Electrochem. 8 (2004) 578, https://doi.org/10.1007/s10008-003-0486-5.

[8] S. Diethelm, J. Van herle, J. Sfeir, P. Buffat, Correlation between oxygen transport properties and microstructure in $La_{0.5}Sr_{0.5}FeO_{3-\delta}$, J. Eur. Ceram. Soc. 25 (2005) 2191–2196, https://doi.org/10.1016/j.jeurceramsoc.2005.03.028.

[9] E.V. Tsipis, M.V. Patrakeev, V.V. Kharton, A.A. Yaremchenko, G.C. Mather, A. L. Shaula, I.A. Leonidov, V.L. Kozhevnikov, J.R. Frade, Transport properties and

thermal expansion of Ti-substituted $La_{1-x}Sr_xFeO_{3-\delta}$ (x = 0.5–0.7), Solid State Sci. 7 (2005) 355–365, https://doi.org/10.1016/j.solidstatesciences.2005.01.001.
[10] H. Bae, J. Hong, B. Singh, A.K. Srivastava, J.H. Joo, S.-J. Song, Investigations on defect equilibrium, thermodynamic quantities, and transport properties of $La_{0.5}Sr_{0.5}FeO_{3-\delta}$, J. Electrochem. Soc. 166 (2019) F180–F189, https://doi.org/10.1149/2.0311904jes.
[11] L.J. Gauckler, D. Beckel, B.E. Buergler, E. Jud, U.P. Muecke, M. Prestat, J.L. M. Rupp, J. Richter, Solid oxide fuel cells: systems and materials, Chimia 58 (2004) 837–850, https://doi.org/10.2533/000942904777677047.
[12] Y. Yin, H. Dai, S. Yu, L. Bi, E. Traversa, Tailoring cobalt-free $La_{0.5}Sr_{0.5}FeO_{3-\delta}$ cathode with a nonmetal cation-doping strategy for high-performance proton-conducting solid oxide fuel cells, SusMat 2 (2022) 607–616, https://doi.org/10.1002/sus2.79.
[13] H. Choi, A. Fuller, J. Davis, C. Wielgus, U.S. Ozkan, Ce-doped strontium cobalt ferrite perovskites as cathode catalysts for solid oxide fuel cells: effect of dopant concentration, Appl. Catal. B Environ. 127 (2012) 336–341, https://doi.org/10.1016/j.apcatb.2012.08.027.
[14] W.D. Penwell, J.B. Giorgi, Conductivity of cerium doped $BaFeO_{3-\delta}$ and applications for the detection of oxygen, Sensor. Actuator. B Chem. 191 (2014) 171–177, https://doi.org/10.1016/j.snb.2013.09.095.
[15] P.-M. Geffroy, J. Fouletier, N. Richet, T. Chartier, Rational selection of MIEC materials in energy production processes, Chem. Eng. Sci. 87 (2013) 408–433, https://doi.org/10.1016/j.ces.2012.10.027.
[16] X. Zhu, H. Wang, W. Yang, Structural stability and oxygen permeability of cerium lightly doped $BaFeO_{3-\delta}$ ceramic membranes, Solid State Ionics 177 (2006) 2917–2921, https://doi.org/10.1016/j.ssi.2006.08.027.
[17] W. Li, Z. Cao, X. Zhu, W. Yang, High-rate hydrogen separation using an MIEC oxygen permeable membrane reactor, AIChE J. 63 (2016) 1278–1286, https://doi.org/10.1002/aic.15502.
[18] X. Zhu, H. Wang, Y. Cong, W. Yang, Partial oxidation of methane to syngas in $BaCe_{0.15}Fe_{0.85}O_{3-\delta}$ membrane reactors, Catal. Lett. 111 (2006) 179–185, https://doi.org/10.1007/s10562-006-0145-4.
[19] H. Liu, K. Zhu, Y. Liu, W. Li, L. Cai, X. Zhu, M. Cheng, W. Yang, Structure and electrochemical properties of cobalt-free perovskite cathode materials for intermediate-temperature solid oxide fuel cells, Electrochim. Acta 279 (2018) 224–230, https://doi.org/10.1016/j.electacta.2018.05.086.
[20] Z. Tao, L. Bi, Z. Zhu, W. Liu, Novel cobalt-free cathode materials $BaCe_xFe_{1-x}O_{3-\delta}$ for proton-conducting solid oxide fuel cells, J. Power Sources 194 (2009) 801–804, https://doi.org/10.1016/j.jpowsour.2009.06.071.
[21] L. Yin, M. Zhang, S. Wang, B. Huang, Y. Du, Heteroatom-driven coordination fields altering single cerium atom sites for efficient oxygen reduction reaction, Advanced matter 35 (2023) 2302485, https://doi.org/10.1002/adma.202302485.
[22] N.E. Trofimenko, H. Ullmann, Oxygen stoichiometry and mixed ionic-electronic conductivity of $Sr_{1-a}Ce_aFe_{1-b}Co_bO_{3-x}$ perovskite-type oxides, J. Eur. Ceram. Soc. 20 (2000) 1241–1250, https://doi.org/10.1016/S0955-2219(99)00292-7.
[23] H. Toby, R.B. Von Dreele, GSAS-II: the genesis of a modern open-source all purpose crystallography software package, J. Appl. Crystallogr. 46 (2013) 544–549, https://doi.org/10.1107/S0021889813003531.
[24] M.V. Patrakeev, I.A. Leonidov, V.L. Kozhevnikov, Applications of coulometric titration for studies of oxygen non-stoichiometry in oxides, J. Solid State Electrochem. 15 (2011) 931–954, https://doi.org/10.1007/s10008-010-1111-z.
[25] M.V. Patrakeev, I.A. Leonidov, V.L. Kozhevnikov, K.R. Poeppelmeier, p-Type electron transport in $La_{1-x}Sr_xFeO_{3-\delta}$ at high temperatures, J. Solid State Chem. 178 (2005) 921–927, https://doi.org/10.1016/j.jssc.2004.10.038.
[26] M.V. Patrakeev, J.A. Bahteeva, E.B. Mitberg, I.A. Leonidov, V.L. Kozhevnikov, K. R. Poeppelmeier, Electron/hole and ion transport in $La_{1-x}Sr_xFeO_{3-\delta}$, J. Solid State Chem. 172 (2003) 219–231, https://doi.org/10.1016/S0022-4596(03)00040-9.
[27] O.V. Merkulov, R.R. Samigullin, A.A. Markov, M.V. Patrakeev, Impact of A-site cation deficiency on charge transport in $La_{0.5-x}Sr_{0.5}FeO_{3-\delta}$, Materials 14 (20) (2021) 5990, https://doi.org/10.3390/ma14205990.
[28] R.D. Shannon, Revised effective ionic radii and systematic studies of interatomic distances in halides and chalcogenides, Acta Crystallogr., Sect. A 32 (1976) 751–767, https://doi.org/10.1107/S0567739476001551.
[29] M.T. Colomer, B.C.H. Steele, J.A. Kilner, Structural and electrochemical properties of the $Sr_{0.8}Ce_{0.1}Fe_{0.7}Co_{0.3}O_{3-\delta}$ perovskite as cathode material for ITSOFCs, Solid State Ionics 147 (2002) 41–48, https://doi.org/10.1016/S0167-2738(02)00002-4.
[30] V.V. Kharton, A.A. Yaremchenko, M.V. Patrakeev, E.N. Naumovich, F.M. B. Marques, Thermal and chemical induced expansion of $La_{0.3}Sr_{0.7}(Fe,Ga)O_{3-\delta}$ ceramics, J. Eur. Ceram. Soc. 23 (2003) 1417–1426, https://doi.org/10.1016/S0955-2219(02)00308-4.
[31] N.H. Perry, J.J. Kim, S.R. Bishopab, H.L. Tuller, Strongly coupled thermal and chemical expansion in the perovskite oxide system $Sr(Ti,Fe)O_{3-\alpha}$, J. Mater. Chem. A 3 (2015) 3602–3611, https://doi.org/10.1039/c4ta05247a.
[32] D. Bayraktar, S. Diethelm, T. Graule, J. Van herle, P. Holtappels, Properties of B-site substituted $La_{0.5}Sr_{0.5}FeO_{3-\delta}$ perovskites for application in oxygen separation membranes, J. Electroceram. 22 (2009) 55–60, https://doi.org/10.1007/s10832-008-9428-z.
[33] K.Yu Chesnokov, A.A. Markov, M.V. Patrakeev, I.A. Leonidov, A.M. Murzakaev, O. N. Leonidova, E.V. Shalaeva, V.V. Kharton, V.L. Kozhevnikov, Structure and transport properties of $La_{0.5}Sr_{0.5-x}Ca_xFeO_{3-\delta}$, Solid State Ionics 262 (2014) 672–677, https://doi.org/10.1016/j.ssi.2013.11.050.
[34] V.V. Kharton, J.C. Waerenborghc, A.P. Viskup, S.O. Yakovlev, M.V. Patrakeev, P. Gaczyński, I.P. Marozau, A.A. Yaremchenko, A.L. Shaula, V.V. Samakhval, Mixed conductivity and Mössbauer spectra of $(La_{0.5}Sr_{0.5})_{1-x}Fe_{1-y}Al_yO_{3-\delta}$. (x = 0-0.05, y = 0-0.30), J. Solid State Chem. 179 (2006) 1273–1284, https://doi.org/10.1016/j.jssc.2006.01.037.
[35] A.A. Markov, S.S. Nikitin, O.V. Merkulov, M.V. Patrakeev, Exploring the defect equilibrium and charge transport in electrode material $La_{0.5}Sr_{0.5}Fe_{0.9}Mo_{0.1}O_{3-\delta}$, Phys. Chem. Chem. Phys. 24 (2022) 21892–21903, https://doi.org/10.1039/d2cp02875a.
[36] A.A. Markov, S.S. Nikitin, B.V. Politov, E.V. Shalaeva, A.P. Tyutyunnik, I. A. Leonidov, M.V. Patrakeev, The impact of cerium content on oxygen stoichiometry, defect equilibrium, and thermodynamic quantities of $Sr_{1-x}Ce_xFeO_{3-\delta}$, J. Alloys Compd. 875 (2021) 160051 https://doi.org/10.1016/j.jallcom.2021.160051.
[37] Non-linear least-squares minimization and curve-fitting for Python. https://lmfit.github.io/lmfit-py (accessed 1 November 2023).
[38] S.S. Nikitin, A.A. Markov, I.A. Leonidov, M.V. Patrakeev, Impact of cerium content on ion and electron transport in $Sr_{1-x}Ce_xFeO_{3-\delta}$, J. Phys. Chem. C 125 (2021) 17546–17555, https://doi.org/10.1021/acs.jpcc.1c05144.
[39] S.S. Nikitin, O.V. Merkulov, I.A. Leonidov, M.V. Patrakeev, High-temperature charge transport in $Nd_{0.25}Sr_{0.75}FeO_{3-\delta}$: the influence of various factors, Dalton Trans. 50 (2021) 11429–11439, https://doi.org/10.1039/d1dt02050a.
[40] Y. Ikuma, S. Anandan, K. Niwa, Lattice parameter, defect concentration and oxygen diffusion in ceria solid solutions, Trans. Mater. Res. Soc. Jpn. 35 (2010) 485–489, https://doi.org/10.14723/tmrsj.35.485.
[41] Y. Ikuma, K. Takao, M. Kamiya, E. Shimada, X-ray study of cerium oxide doped with gadolinium oxide fired at low temperatures, Mater. Sci. Eng. B 99 (2003) 48–51, https://doi.org/10.1016/S0921-5107(02)00546-9.
[42] P. Xiaokaiti, T. Yu, A. Yoshida, G. Guan, A. Abudula, Evaluation of cerium doped perovskites $(Ce_{0.1}Sr_{0.9})_xCo_{0.3}Fe_{0.7}O_{3-\delta}$ as cathode materials for solid oxide fuel cells, Catal. Today 332 (2019) 94–100, https://doi.org/10.1016/j.cattod.2018.08.017.
[43] A.M. Svensson, S. Sunde, K. Nisşancioğlu, Mathematical modeling of oxygen exchange and transport in air-perovskite-YSZ interface regions: I. Reduction of intermediately adsorbed oxygen, J. Electrochem. Soc. 144 (1997) 2719, https://doi.org/10.1149/1.1837887.
[44] A.M. Svensson, S. Sunde, K. Nisşancioğlu, Mathematical modeling of oxygen exchange and transport in air-perovskite-YSZ interface regions: II. Direct exchange of oxygen vacancies, J. Electrochem. Soc. 145 (1998) 1390, https://doi.org/10.1149/1.1838471.
[45] K.K. Hansen, Evaluation of LSF based SOFC cathodes using cone-shaped electrodes and EIS, Solid State Ionics 344 (2020) 115096, https://doi.org/10.1016/j.ssi.2019.115096.
[46] F. Bidrawn, S. Lee, J.M. Vohs, R.J. Gorte, The effect of Ca, Sr, and Ba doping on the ionic conductivity and cathode performance of $LaFeO_3$, J. Electrochem. Soc. 155 (2008) B660–B665, https://doi.org/10.1149/1.2907431.
[47] Y. Takeda, R. Kanno, M. Noda, Y. Tomida, O. Yamamoto, Cathodic polarization phenomena of perovskite oxide electrodes with stabilized zirconia, J. Electrochem. Soc. 134 (1987) 2656, https://doi.org/10.1149/1.2100267.